International Forum on Aeroelasticity and Structural Dynamics
IFASD 2019
9-13 June 2019, Savannah, Georgia, USA

ASSESSMENT OF T-TAIL FLUTTER USING AN ENHANCED POTENTIAL FLOW THEORY APPROACH AND LINEARIZED FREQUENCY DOMAIN CFD DATA

Dominik Schäfer[1], Jürgen Arnold[1]

[1] DLR – German Aerospace Center
Institute of Aeroelasticity
Bunsenstraße 10, 37073 Göttingen Germany
D.Schaefer@dlr.de

Keywords: T-tail flutter, unsteady aerodynamics, linearized frequency domain solver, strip theory.

Abstract: This paper aims at assessing the gain in accuracy for T-tail flutter point prediction obtained by a strip theory approach used to enhance common linear potential flow theory based unsteady aerodynamic forces. The common approach neglects unsteady aerodynamic forces induced by lifting surface inplane and roll motion, which are crucial for T-tail flutter. The strip theory approach computes these additional terms based on aerodynamic forces from a steady state reference condition and the modal data of the underlying structural model. The correction is done by superposing the additional terms with the aerodynamic forces from the standard procedure. Generalized aerodynamic forces produced by the common approach and the enhanced approach in addition to resulting flutter points and aerodynamic Modal Power Transfer matrices are compared to those computed with aerodynamic forces from the linearized frequency domain CFD solver TAU-LFD. Two Mach numbers of 0.4 and 0.69 are chosen for this assessment. The model for the study is a generic T-tail with unswept and non-tapered vertical and horizontal tail planes. Significant improvements of the flutter points of the T-tail for both Mach numbers can be achieved by the enhancement in relation to the CFD approach. A comparison of generalized aerodynamic forces and aerodynamic Modal Power Transfer values, however, reveals strengths and weaknesses of the method.

1 INTRODUCTION

The ambitious visions for future air transport beyond 2020 involve quieter and cleaner engines on large passenger aircrafts, causing next generation power plants to grow in diameter in order to increase the bypass ratio. This necessitates the review of their mounting positions, since the engines must allow sufficient ground clearance to avoid contact with the runway as well as foreign object ingestion. A potential solution to this problem is mid- to rear fuselage-mounted engines, which renders the use of conventional tail units unfavorable. Instead, alternative tail designs, e.g. T-tails and H-tails, are preferred. However, these tail designs feature adverse flutter characteristics involving physical effects, which are usually not covered by standard flutter assessment processes. These include, for instance, unsteady aerodynamic forces caused by horizontal stabilizer roll and inplane motion.

One way to add these terms to the flutter process is to compute them externally and superpose them with the commonly obtained aerodynamic forces. In [1, 2], a strip theory approach is described which uses steady aerodynamic forces in addition to the modal data of the structural model to compute these terms and include them in the flutter process.

This paper aims at assessing the gain in accuracy for flutter point prediction obtained by the external method in relation to the standard potential flow theory based method and linearized frequency domain CFD data.

2 METHODS

2.1 General approach

The modal properties of the structural model are determined by real eigenvalue extraction using the solution sequence SOL 103 provided by Nastran. The generalized mass and stiffness matrices as well as the structural eigenmodes form the basis for the subsequent aerodynamic and flutter analyses.

The linear potential flow theory method ZONA6, which is available in the aeroelastic software package ZAERO, is used for the generation of generalized aerodynamic forces (GAFs) representing the common approach. Steady aerodynamic forces from CFD computations at different horizontal tail plane (HTP) incidence angles are used for the improvement of the GAFs using the strip theory approach. For this, the steady aerodynamic CFD forces are interpolated on the strip model. After computing the additional motion induced aerodynamic forces, they are being generalized and superposed with the conventionally obtained GAFs according to the assumption of linearity. The resulting matrices are read by ZAERO for the solution of the g-method flutter equation.

The gain in accuracy is assessed by comparing the GAF matrix entries used for the flutter process input, the resulting flutter points, and aerodynamic Modal Power Transfer (MPT) matrix entries with linearized frequency domain (LFD) CFD data at subsonic and low transonic Mach numbers of 0.4 and 0.69, respectively. For the CFD approach, the linearized frequency domain solver TAU-LFD [3] is used with an unstructured mesh for inviscid compressible simulations in Euler mode. The structural mode shapes are interpolated on the CFD surface mesh using the Thin Plate Spline (TPS) method. The CFD approach requires the determination of the aerodynamic response by excitation of each structural mode at a set of predefined reduced frequencies with a sinusoidal deformation input. As in the case of the enhanced GAFs, the resulting CFD-based GAF matrices are read by ZAERO for the solution of the flutter equation.

2.2 Nastran SOL 103

The modal analysis for obtaining the generalized mass and stiffness matrices is performed using the solution sequence SOL 103 provided by Nastran [4]. By applying the Lanczos method, the real eigenvalue problem (Eq. (1)) is solved for the elastic structural modes. Here, $\bar{\boldsymbol{K}}$ denotes the structural stiffness matrix and $\bar{\boldsymbol{M}}$ the structural mass matrix in physical degrees of freedom. $\lambda_i = \omega_i^2$ is the real eigenvalue and $\boldsymbol{\phi}_i$ the corresponding real eigenvector.

$$([\bar{\boldsymbol{K}} - \lambda_i \bar{\boldsymbol{M}}])\boldsymbol{\phi}_i = 0 \tag{1}$$

Combining the real eigenvectors $\boldsymbol{\phi}_i$ into a mode shape matrix $\boldsymbol{\Phi}$ with

$$\boldsymbol{\Phi} = [\boldsymbol{\phi}_1, \boldsymbol{\phi}_2, \dots, \boldsymbol{\phi}_n] \tag{2}$$

and n being the number of mode shapes, the generalized mass and stiffness matrices in modal degrees of freedom are obtained by

$$\boldsymbol{M} = \boldsymbol{\Phi}^T \overline{\boldsymbol{M}} \boldsymbol{\Phi} \tag{3}$$

$$\boldsymbol{K} = \boldsymbol{\Phi}^T \overline{\boldsymbol{K}} \boldsymbol{\Phi} \tag{4}$$

2.3 ZAERO ZONA6

The software package ZAERO provides the ZONA6 method, which is used for the computation of subsonic unsteady aerodynamic forces based on the linearized small-disturbance potential flow theory [5]. The method solves the steady and unsteady three-dimensional linearized small disturbance potential equations (LSDPE), which read

$$(1 - M_\infty^2)\varphi_{0xx} + \varphi_{0yy} + \varphi_{0zz} = 0 \tag{5}$$

$$(1 - M_\infty^2)\varphi_{1xx} + \varphi_{1yy} + \varphi_{1zz} - 2\frac{M_\infty}{a_\infty}\varphi_{1xt} - \frac{1}{a_\infty^2}\varphi_{1tt} = 0 \tag{6}$$

where M_∞ is the freestream Mach number, a_∞ the speed of sound, and φ_0 and φ_1 the steady and unsteady potentials, respectively. The subscripts indicate the partial differentiation of the potentials, e.g. $\varphi_{0xx} = \partial^2\varphi_0/\partial x^2$. Eq. (5) is the steady and Eq. (6) the unsteady LSDPE. By assuming simple harmonic motion with constant amplitude, Eq. (6) can be transformed into an integral equation which is then solved by utilizing the panel method. After subdividing the configuration into lifting surface and body panels and further into small quadrilaterals (aerodynamic boxes), this method establishes the aerodynamic influence coefficient matrices $\boldsymbol{AIC}(\mathrm{j}k, M)$, which relate the downwash at each aerodynamic box to the pressure coefficient differences at the aerodynamic boxes for each pair of Mach number M and reduced frequency k, viz.

$$\Delta\boldsymbol{c_p} = \boldsymbol{AIC^T}(\mathrm{j}k, M)\boldsymbol{w} \tag{7}$$

with $\mathrm{j} = \sqrt{-1}$. The reduced frequency is

$$k = \frac{\omega\bar{c}}{2V} \tag{8}$$

with ω being the angular frequency of the oscillation, V the reference velocity, and $\bar{c}$ the reference chord length.

The resulting aerodynamic forces $\boldsymbol{F_a}$ are being generalized by the modal matrix at aerodynamic degrees of freedom (DoF) $\boldsymbol{\Phi_a}$ according to

$$\boldsymbol{Q}(\mathrm{j}k, M) = \boldsymbol{\Phi_a}^T \boldsymbol{F_a} = \boldsymbol{\Phi}^T\, \boldsymbol{G}_{1/4}^T\, \boldsymbol{S}\, \boldsymbol{AIC}^T(\mathrm{j}k, M)\, \boldsymbol{W} \tag{9}$$

Here, the unsteady pressures at the aerodynamic boxes are evaluated from the downwash matrix $\boldsymbol{W}$ at their three quarter chord points, while the generalization of the unsteady aerodynamic forces uses the modal deformations at structural DoF interpolated to the aerodynamic boxes' quarter chord points via the spline matrix $\boldsymbol{G}_{1/4}$. The integration matrix $\boldsymbol{S}$ relates the aerodynamic box pressures to the aerodynamic forces at the quarter chord line.

2.4 TAU-LFD

The linearized frequency domain (LFD) solver implemented in the DLR TAU code [3, 6] is used for small perturbation simulations w.r.t. a (nonlinear) reference state with linearized Euler and Navier-Stokes equations. The RANS equations are written in the form

$$\frac{d}{dt}|\boldsymbol{\Omega}|\boldsymbol{w} + \boldsymbol{r}(\boldsymbol{w}, \boldsymbol{x}, \dot{\boldsymbol{x}}) = 0 \tag{10}$$

with $\boldsymbol{\Omega}$ as a diagonal matrix containing the cell volumes, $\boldsymbol{w} = \rho(1, u, v, w, E, \nu)^T$ as the vector of fluid unknowns, $\boldsymbol{x}$ as a vector of grid coordinates, and $\boldsymbol{r}$ as the residual function with

$$\boldsymbol{r} = \int_{\partial\Omega} \boldsymbol{f_c}(\boldsymbol{w}) \cdot \boldsymbol{n} - \boldsymbol{f_v}(\boldsymbol{w}) \cdot \boldsymbol{n} - \boldsymbol{w}\dot{\boldsymbol{x}} \cdot \boldsymbol{n} - \int_{\Omega} \boldsymbol{q_s} \tag{11}$$

$\boldsymbol{f_c}(\boldsymbol{w}) \cdot \boldsymbol{n}$ is the convective and $\boldsymbol{f_v}(\boldsymbol{w}) \cdot \boldsymbol{n}$ the viscous flux, while $\boldsymbol{n}$ denotes the surface normal vector and $\boldsymbol{q_s}$ the turbulent source vector. For the linearization, the grid motion $\boldsymbol{x}$ and the vector of fluid unknowns $\boldsymbol{w}$ are regarded as the sum of a time-independent mean part and a comparatively small time-dependent perturbation, namely

$$\boldsymbol{w} = \bar{\boldsymbol{w}} + \Delta\boldsymbol{w} \tag{12}$$

$$\boldsymbol{x} = \bar{\boldsymbol{x}} + \Delta\boldsymbol{x} \tag{13}$$

By assuming a dynamically linear system with $\boldsymbol{r}\left(\bar{\boldsymbol{w}}, \bar{\boldsymbol{x}}, \dot{\bar{\boldsymbol{x}}}\right) = 0$, Eq. (10) becomes

$$|\bar{\boldsymbol{\Omega}}| \frac{d}{dt}\Delta\boldsymbol{w} + \left.\frac{\partial \boldsymbol{r}}{\partial \boldsymbol{w}}\right|_{\bar{\boldsymbol{w}},\bar{\boldsymbol{x}},\boldsymbol{0}} \Delta\boldsymbol{w} = -\left.\frac{\partial \boldsymbol{r}}{\partial \boldsymbol{x}}\right|_{\bar{\boldsymbol{w}},\bar{\boldsymbol{x}},\boldsymbol{0}} \Delta\boldsymbol{x} - \left.\frac{\partial \boldsymbol{r}}{\partial \dot{\boldsymbol{x}}}\right|_{\bar{\boldsymbol{w}},\bar{\boldsymbol{x}},\boldsymbol{0}} \Delta\dot{\boldsymbol{x}} - \bar{\boldsymbol{w}}\frac{d}{dt}|\boldsymbol{\Delta\Omega}| \tag{14}$$

Regarding harmonic grid motion and applying the Laplace transformation with $s = \delta + i\omega$ yields the perturbation vectors of fluid unknowns and grid displacements

$$\Delta\mathbf{w} = \hat{\boldsymbol{w}}\mathrm{e}^{st} \tag{15}$$

$$\Delta\mathbf{x} = \hat{\boldsymbol{x}}\mathrm{e}^{st} \tag{16}$$

$$\Delta\dot{\mathbf{x}} = s\hat{\boldsymbol{x}}\mathrm{e}^{st} \tag{17}$$

These considerations yield the linear system of equations

$$\left(s|\bar{\boldsymbol{\Omega}}| + \left.\frac{\partial \boldsymbol{r}}{\partial \boldsymbol{w}}\right|_{\bar{\boldsymbol{w}},\bar{\boldsymbol{x}},\boldsymbol{0}}\right)\hat{\boldsymbol{w}} = -\left.\frac{\partial \boldsymbol{r}}{\partial \boldsymbol{x}}\right|_{\bar{\boldsymbol{w}},\bar{\boldsymbol{x}},\boldsymbol{0}} \hat{\boldsymbol{x}} - s\left(\left.\frac{\partial \boldsymbol{r}}{\partial \dot{\boldsymbol{x}}}\right|_{\bar{\boldsymbol{w}},\bar{\boldsymbol{x}},\boldsymbol{0}} \hat{\boldsymbol{x}} + \bar{\boldsymbol{w}}\left|\hat{\boldsymbol{\Omega}}\right|\right) \tag{18}$$

The residual Jacobian $\partial\boldsymbol{r}/\partial\boldsymbol{w}$ on the left hand side of Eq. (18) is computed analytically, while the right hand side is solved for by applying a central difference scheme with a deformed mesh at positive as well as negative grid deformation amplitude. For the propagation of the surface mesh deformation into the grid volume, Radial basis functions are used [7, 8].

In comparison with full nonlinear CFD computations, the increase in computational performance comes with a loss of accuracy when nonlinear aerodynamic effects are induced by the small perturbations.

2.5 AiM

For the augmentation of the standard linear potential flow theory based unsteady aerodynamic forces for lifting surface inplane and roll motion, a strip theory approach after [1, 2] is chosen. For consistency with [2], this method is called "AiM" (Airbus Military). Steady aerodynamic forces from CFD computations at different HTP incidence angles are interpolated on the strip model, which allows the computation of differential unsteady aerodynamic forces due to strip roll and inplane motion, Eqs. (19) and (20). The side force component due to horizontal tail plane roll as well as out-of-plane bending can be accounted for by

$$\Delta f_y(y,t) = -l(y) * \varphi(t) \tag{19}$$

where the steady lift on each strip $l(y)$ is multiplied by the instantaneous roll angle $\varphi(t)$. The unsteady lift due to inplane motion is described by

$$\Delta f_z(y,t) = C(k)\left[\frac{\partial l(y)}{\partial \beta}\left(\psi_0 + \frac{2\mathrm{j}k\eta_{y0}}{\bar{c}}\right) - 2l(y)\frac{2\mathrm{j}k(\eta_{x0} + y\psi_0)}{\bar{c}}\right] \tag{20}$$

$$\frac{\partial l(y)}{\partial \beta} = \pm l(y)\tan(\Lambda) - \frac{3}{4}c(y)\frac{\partial l(y)}{\partial y} \tag{21}$$

$C(k)$ is Theodorsen's lift deficiency function [9], k the reduced frequency parameter, Λ the strip quarter chord sweep angle, $c(y)$ the strip chord length at strip mid span, ψ_0 the sideslip angle amplitude resulting from the mode motion, η_{y0} the amplitude of the lateral displacement, and η_{x0} the amplitude of the longitudinal displacement. $\bar{c}$ is the reference chord length. The first term in Eq. (20) is the change in steady lift due to sideslip as well as yaw angle and is based on the work of Queijo [10], while the second term is the change in steady lift due to strip velocity parallel to the flow induced by the structural mode.

After computing the additional terms, the force vectors are generalized and superposed with the conventionally obtained generalized aerodynamic forces by the ZONA6 method according to the assumption of linearity, Eq. (22).

$$\boldsymbol{Q_{hh}} = \boldsymbol{Q_{hh}^{\mathrm{ZONA6}}} + \boldsymbol{\Delta Q_{hh}^{\mathrm{T-tail}}} \tag{22}$$

2.6 ZAERO g-Method

The generalized aerodynamic forces obtained by the methods described in Sections 2.3 to 2.5 are valid only for simple harmonic motion and, thus, only at flutter onset. Below and above this point, the g-Method [11] assumes a formulation of the generalized aerodynamic forces for small damping values g according to

$$\boldsymbol{Q}(p) \approx \boldsymbol{Q}(\mathrm{j}k) + g\boldsymbol{Q}'(\mathrm{j}k) \tag{23}$$

With q_∞ as the freestream dynamic pressure, g as the damping factor, $p = g + \mathrm{j}k$, and negligence of structural damping, the assumption leads to the g-method flutter equation, viz.

$$[g^2\boldsymbol{A} + g\boldsymbol{B} + \boldsymbol{C}]\boldsymbol{q} = 0 \tag{24}$$

with

$$\boldsymbol{A} = \left(\frac{2V}{\bar{c}}\right)^2 \boldsymbol{M} \tag{25}$$

$$\boldsymbol{B} = 2\mathrm{j}k\left(\frac{2V}{\bar{c}}\right)^2 \boldsymbol{M} - q_\infty \boldsymbol{Q}'(\mathrm{j}k, M) \tag{26}$$

$$\boldsymbol{C} = -k^2\left(\frac{2V}{\bar{c}}\right)^2 \boldsymbol{M} + \boldsymbol{K} - q_\infty \boldsymbol{Q}(\mathrm{j}k, M) \tag{27}$$

For a solution of Eq. (24), where the damping factor g is real valued, it is rewritten in state-space form

$$[\boldsymbol{D} - g\boldsymbol{I}]\boldsymbol{x} = 0 \tag{28}$$

with $\boldsymbol{x}$ being the eigenvector of the state-space system and

$$\boldsymbol{D} = \begin{bmatrix} \boldsymbol{0} & \boldsymbol{I} \\ -\boldsymbol{A}^{-1}\boldsymbol{C} & -\boldsymbol{A}^{-1}\boldsymbol{B} \end{bmatrix} \tag{29}$$

A reduced frequency sweep then searches for a sign change in $\mathrm{Im}(g)$ with increasing reduced frequency. At the sign change, the flutter frequency and damping values are computed based on a linearly interpolated reduced frequency.

2.7 Aerodynamic Modal Power Transfer

For an evaluation of aerodynamic methods for flutter assessment it is of interest to investigate the aerodynamic Modal Power Transfer (MPT) related to the modes involved in the flutter mechanism [12, 13, 14]. For this, the average power of a periodic motion is considered with T being the oscillation period, $f(t)$ the time-dependent force and $v(t)$ the unsteady motion velocity (Eq. (30)).

$$P = \frac{1}{T}\int_0^T f(t)v(t)dt \tag{30}$$

At flutter onset, the simple harmonic form of the motion allows rewriting Eq. (30) to

$$\boldsymbol{P} = \frac{1}{2}\rho V^2 * \omega_f * \mathrm{Im}\left(\Xi^H \boldsymbol{Q_{hh}}(\mathrm{j}k_f, M_f)\Xi\right) \tag{31}$$

with density ρ, velocity V, flutter angular frequency ω_f, the generalized aerodynamic forces matrix at the flutter crossing $\boldsymbol{Q_{hh}}(\mathrm{j}k_f, M_f)$, and the diagonal matrix Ξ of the modal flutter eigenvector. In this way, a matrix $\boldsymbol{P}$ can be established where each entry reflects the aerodynamic MPT between an excited mode (column) and an affected mode (row). Adding up the unsigned matrix elements column by column yields an indication for the relevance of each mode for the flutter mechanism in terms of its aerodynamic contribution. In turn, the sum of all signed matrix elements should result in a value close to zero at flutter onset.

3 SIMULATION MODELS

The configuration for this study is a generic T-tail with unswept and non-tapered vertical and horizontal tail planes after [2] (Figure 1). The simplicity of the model facilitates a fast method development and provides an opportunity for a comparison with literature data.

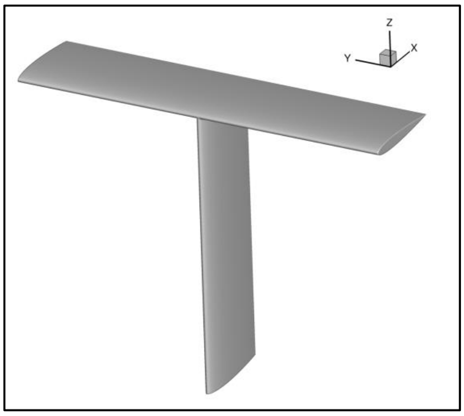

Figure 1: Generic T-tail configuration after Murua [2]

3.1 Structural model

The structural model properties (Table 1) are chosen according to [2], which leads to a vertical tail plane (VTP) out-of-plane bending frequency of 2.85Hz and a VTP torsional frequency of 5.28Hz. The first structural mode results in an HTP roll motion with a low amount of yaw while the second mode yields an HTP inplane motion with a low amount of roll. The mode shapes at aerodynamic degrees of freedom are displayed in Figure 4 and Figure 5.

Table 1: Geometric and structural properties of the generic T-tail after Murua [2]

	VTP	HTP
Chord	2.0m	2.0m
Root-to-tip distance	6.0m	4.0m
Elastic axis (from L.E.)	25% chord	25% chord
Center of gravity (from L.E.)	35% chord	35% chord
Mass per unit length	35 kg/m	35 kg/m
Sectional moment of inertia per unit length (around E.A.)	8 kg*m	8 kg*m
Torsional stiffness, GJ	1.0E+07 Nm²	1.0E+10 Nm²
Out-of-plane bending stiffness, EI_1	1.0E+07 Nm²	1.0E+10 Nm²
Inplane bending stiffness, EI_2	∞	∞

3.2 DLM model

For the computation of unsteady aerodynamic forces with linear potential flow theory, a panel representation of the geometry is used with an aerodynamic box distribution as shown in Figure 2.

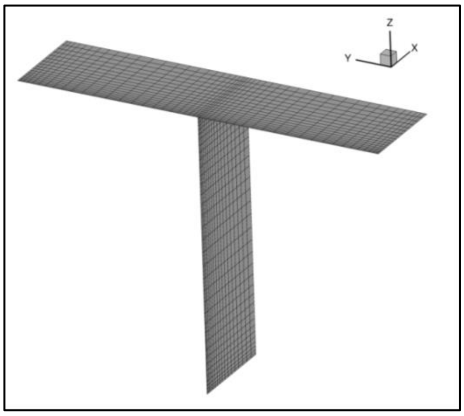

Figure 2: Panel discretization of the generic T-tail

The depicted discretization is a result of a steady as well as an unsteady mesh convergence study performed with four different mesh sizes (Table 2). Here, the parameter NC is the number of chordwise aerodynamic boxes, while the parameter NS is the number of spanwise boxes. N gives the total number of aerodynamic boxes. An estimation for the aerodynamic box chord length may be obtained by [15]

$$x < \frac{\bar{c}}{12} \frac{\pi}{k\left(\frac{M}{\beta}\right)^2} \tag{32}$$

x denotes the required minimum box chord length, $\bar{c}$ the reference chord length, k the reduced frequency, M the Mach number, and $\beta = \sqrt{|M^2 - 1|}$.

With the reduced frequency for the present case ranging from 0.0 to 1.0 and a max. considered Mach number of $M = 0.69$, the required minimum aerodynamic box chord length amounts to 0.341m, which results in 6 chordwise boxes for the VTP and the HTP, respectively. To maintain a reasonable aerodynamic box aspect ratio, the VTP is discretized by 12 and the HTP by 16 spanwise boxes.

Table 2: DLM mesh convergence study; 2.0° angle of incidence

Label	NC	NS VTP/HTP	N	M=0.40			M=0.69		
				C_L / -	V_F / (m/s)	k_F / -	C_L / -	V_F / (m/s)	k_F / -
Coarse	6	12/16	168	0.138	239.566	0.133	0.156	260.002	0.120
Medium	12	24/32	672	0.135	248.719	0.127	0.152	269.492	0.116
Fine	24	48/64	2688	0.134	253.747	0.125	0.151	274.687	0.113
Very fine	36	72/96	6048	0.133	255.634	0.124	0.150	276.636	0.112
Final	18	36/48	1512	0.135	252.708	0.125	0.152	273.421	0.114

The steady lift coefficients and flutter velocities converge for the very fine mesh with a relative error below 1%, but the discretization level is computationally too expensive. The mesh labelled “Medium” fulfills the discretization requirements outlined above and leads to relative static lift coefficient errors below 1.5% w.r.t. the very fine mesh and relative flutter velocity errors of about -2.7%. An increased aerodynamic box density at the leading edges in chordwise direction and at the lifting surface roots and tips in spanwise direction leads to the finally used discretization (“Final”), as the steady lift coefficients and flutter points show a relative error of approximately 1% to the very fine mesh. With less aerodynamic boxes compared to the very fine mesh, the computational performance is suitable for the present study. Furthermore, this discretization is more convenient for an interpolation of steady CFD pressures due to the higher number of aerodynamic boxes at the lifting surface leading edges and at the junction between HTP and VTP.

3.3 CFD model

An unstructured mesh with approximately 0.2 million grid points and 1.1 million tetrahedra elements (Figure 3) is used for the computation of the linearized aeroelastic transfer matrices w.r.t. a nonlinear, inviscid aerodynamic reference state using the Euler equations.

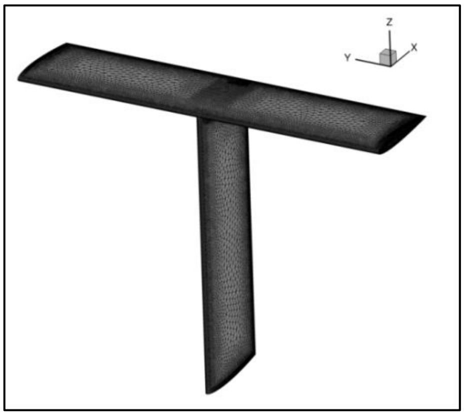

Figure 3: CFD surface mesh of the generic T-tail

Due to the high computational effort, the mesh convergence study is limited to steady state conditions at Mach numbers of 0.40 and 0.69 (Table 3). The total number of tetrahedral elements, denoted by N, varies between 0.6 million and 2.9 million. The mesh labelled “Medium” is used for the presented assessment.

Table 3: CFD mesh convergence study; 2.0° angle of incidence

Label	$\mathrm{N} * 1E6$	Mach 0.40				Mach 0.69			
		C_L / -	ΔC_L / %	C_m / -	ΔC_m / %	C_L / -	ΔC_L / %	C_m / -	ΔC_m / %
Coarse	0.6	0.1076	1.128	0.0227	5.093	0.1082	0.464	0.0321	15.884
Medium	1.1	0.1068	0.376	0.0208	-3.704	0.1072	-0.464	0.0295	6.498
Fine	2.9	0.1064	-	0.0216	-	0.1077	-	0.0277	-

3.4 Aeroelastic model

Structural deformations are interpolated on the DLM model with the Infinite Plate Spline (IPS) method and on the CFD model with the Thin Plate Spline (TPS) method. The interpolated two mode shapes, namely the VTP out-of-plane bending (Mode 1) and the VTP torsion (Mode 2), are displayed in Figure 4 and Figure 5.

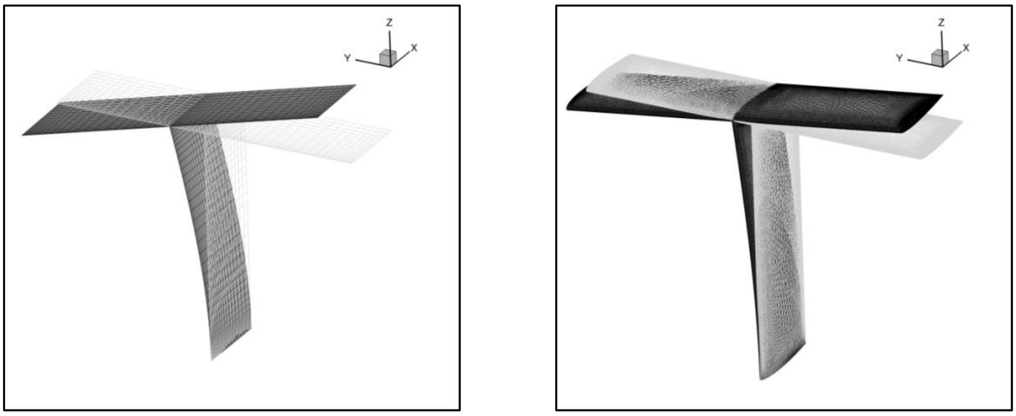

Figure 4: Mode 1 interpolated on DLM mesh (left) and on CFD mesh (right)

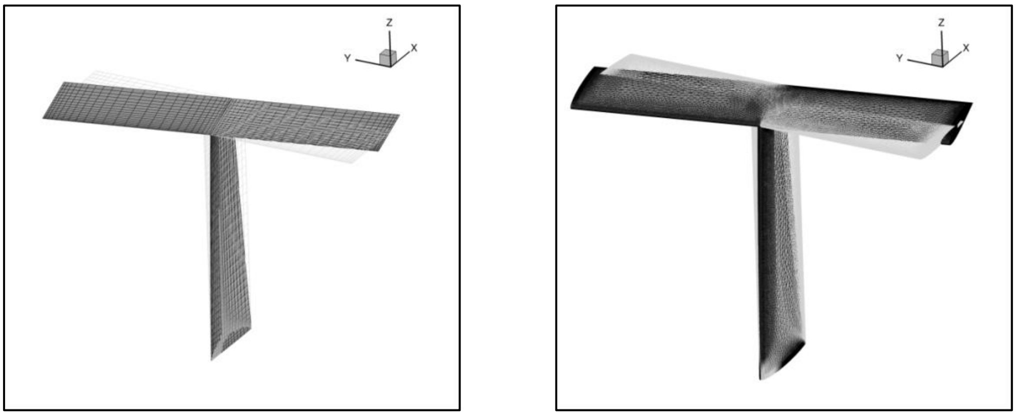

Figure 5: Mode 2 interpolated on DLM mesh (left) and on CFD mesh (right)

4 RESULTS

All computations are carried out with an HTP angle of incidence of 2°. The reference density and reference temperature correspond to the definitions of the international standard atmosphere at mean sea level and amount to 1.225kg/m³ and 288.15K, respectively [16]. The reference chord length is 2.0m, while half the reference chord length is chosen for the reduced frequency (Eq. (8)). The reference span amounts to 8.0m and the reference area to 16m². All flutter computations are non-matched with fixed Mach number and density while the velocity is variable. A Mach number of 0.4 is chosen for subsonic reference computations with the objective of excluding aerodynamic nonlinearities. In addition, computations are carried out at a Mach number of 0.69, which corresponds to an onset flow Mach number of 0.78 for tail designs with an HTP quarter chord sweep angle of 28°.

4.1 Flutter mechanism

The flutter mechanism of the generic T-tail test case (Figure 6) is common for this kind of tail design. The modal contributions are VTP out-of-plane bending and VTP torsion. These mode shapes, combined with the relatively stiff HTP (cf. Table 1), result in a rigid body motion of the HTP in roll and yaw, respectively.

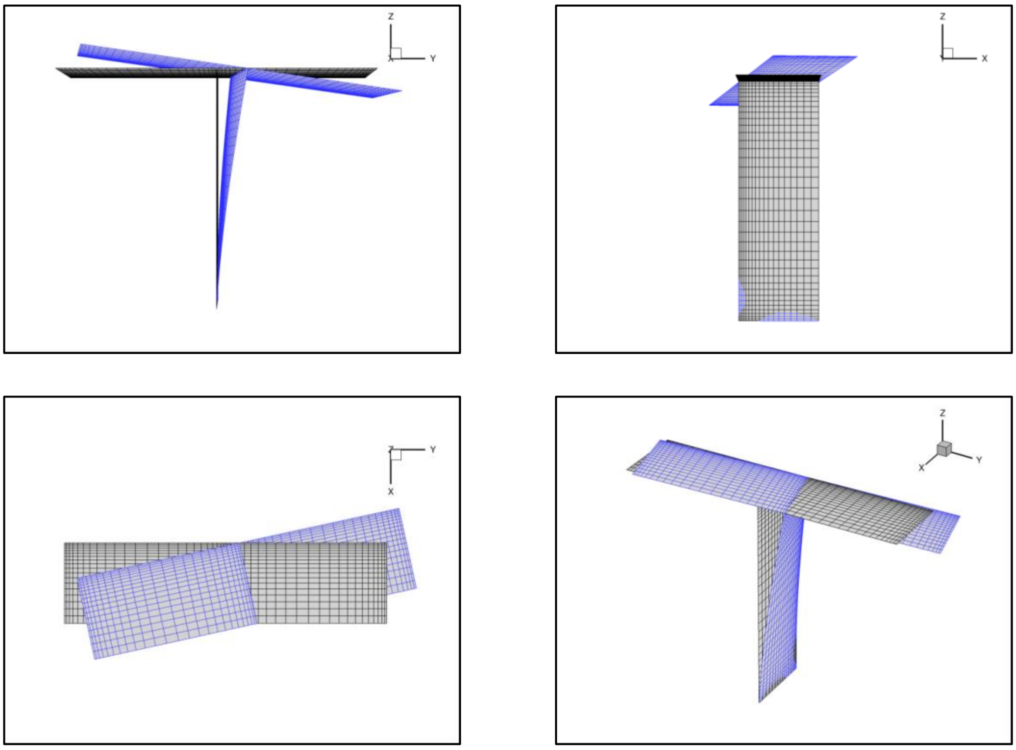

Figure 6: Flutter mechanism of the generic T-tail test case

4.2 Flutter onset

Figure 7 shows a comparison of the damping curves of the VTP torsion mode (Mode 2) computed by solving the g-method flutter equation with generalized aerodynamic forces from the ZONA6 method, TAU-LFD, and the AiM method. In this figure, the dimensionless damping coefficient of the second mode shape is displayed against the onset velocity for non-matched flutter computations at Mach numbers of 0.4 (solid lines) and 0.69 (dashed lines). The corresponding numerical values for the flutter onset are listed in Table 4.

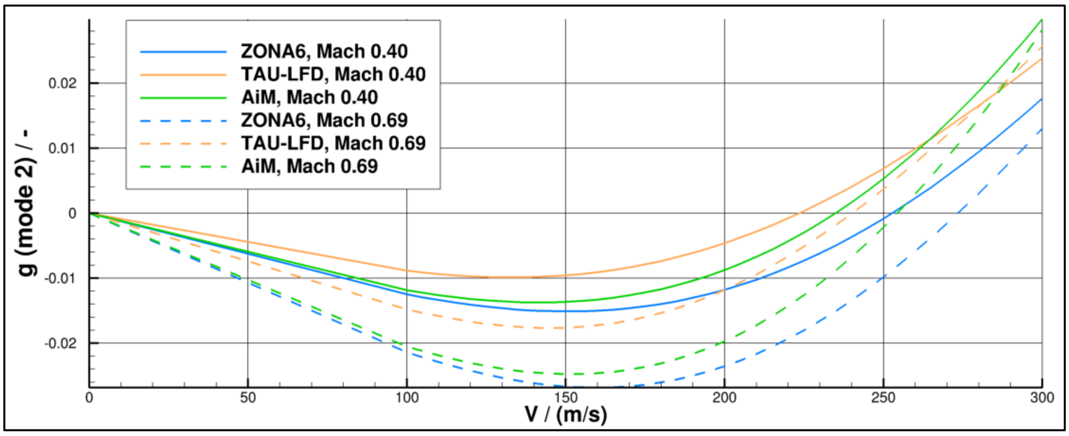

Figure 7: Comparison of damping curves (Mode 2) between ZONA6, TAU-LFD, and AiM at Mach numbers of 0.40 and 0.69

Table 4: Comparison of flutter points between ZONA6, TAU-LFD, and AiM

	$M = 0.40$				M=0.69			
	V_F / (m/s)	ΔV_F / %	f_F / Hz	k_F / -	V_F / (m/s)	ΔV_F / %	f_F / Hz	k_F / -
ZONA6	252.708	13.184	5.043	0.125	273.421	13.925	4.953	0.114
TAU-LFD	223.445	0.000	5.168	0.145	240.139	0.000	5.123	0.134
AiM	234.879	5.117	5.054	0.135	254.346	5.916	4.963	0.123

The common linear potential flow theory based approach predicts the flutter points of the generic T-tail at roughly 253m/s for a Mach number of 0.4 and at 273m/s for a Mach number of 0.69 (Figure 7, Table 4).

The CFD based approach results in lower flutter velocities of 223m/s and 240m/s, respectively, with a deviation of over 13% to the flutter points obtained with ZONA6 GAFs for both Mach numbers. Noteworthy, the computed flutter velocity at a Mach number of 0.69 is close to the velocity on which the generalized aerodynamic forces are based, which therefore corresponds to a matched analysis.

The AiM method significantly alters the potential flow theory based flutter velocities of the generic T-tail. With the strip theory enhancement, the flutter points are predicted to be at 235m/s and 254m/s, respectively. The initial deviations in the flutter velocities w.r.t. the CFD based approach of approximately 13% can be reduced to 5-6% for both Mach numbers.

4.3 Generalized aerodynamic forces

The generalized aerodynamic forces used as input for the flutter process are depicted in Figure 8 and Figure 9 for both Mach numbers. The plots show amplitude and phase angle of the enhanced GAF matrix entries compared to those obtained by the ZONA6 method and TAU-LFD over the range of reduced frequencies. The matrix columns indicate the cause of the aerodynamic response (excited mode) and the matrix rows the affected modes. The reduced frequencies 0.090, 0.146, and 0.236 are outlined in black to indicate the relevant range of this parameter for the flutter point.

For a Mach number of 0.4 (Figure 8), the influence of the AiM approach on the generalized aerodynamic forces induced by both considered modes is significant. While the amplitude of the aerodynamic influence of the VTP out-of-plane bending mode on both modes is not being changed considerably (first figure column), the phase angle is being decreased noticeably. For the aerodynamic influence of the VTP torsion mode on the VTP out-of-plane bending mode (first row, second column, $\boldsymbol{Q_{hh}}(1,2)$) it can be observed that the difference in amplitude between the ZONA6 approach and TAU-LFD can be reduced by the AiM method for those reduced frequencies relevant for the flutter mechanism, but for high reduced frequencies the method yields amplitudes that are too high compared to the values based on TAU-LFD. A slightly decreased phase angle is visible over the entire reduced frequency envelope. The aerodynamic influence of the VTP torsion mode on itself (second row, second column, $\boldsymbol{Q_{hh}}(2,2)$) is not being affected significantly except for a low decrease in phase angle and a low increase in amplitude.

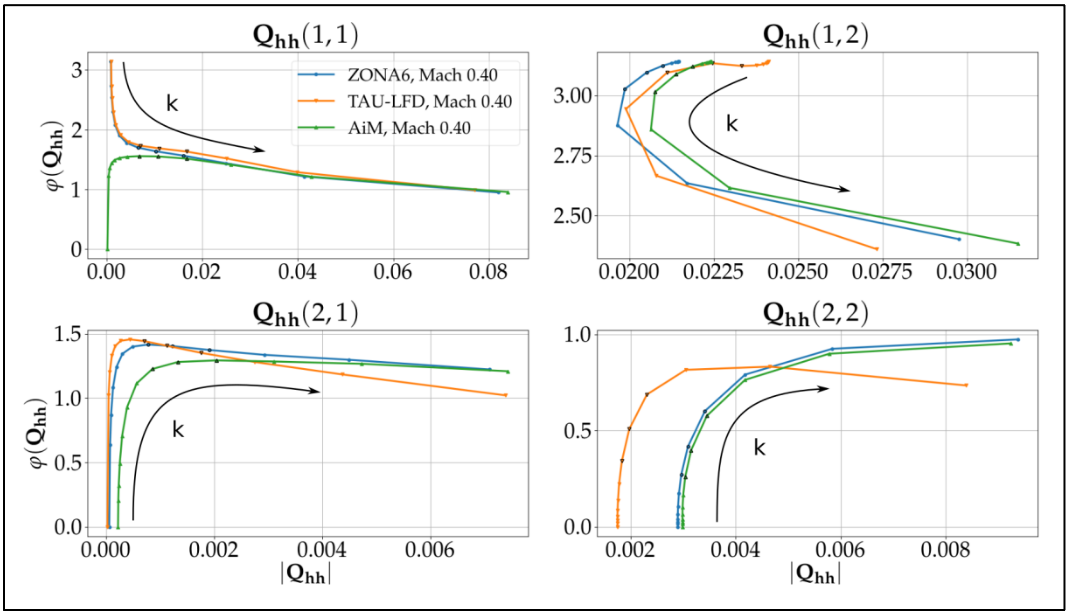

Figure 8: Comparison of GAF matrix entries between ZONA6, TAU-LFD, and AiM at a Mach number of 0.40

For a Mach number of 0.69, the corresponding generalized aerodynamic forces are displayed in Figure 9. While the effect of the AiM approach on the influence of the VTP out-of-plane bending mode on both modes (first figure column) is comparable to that for a Mach number of 0.4 (cf. Figure 8), the deviations concerning the influence of the VTP torsion mode on the VTP out-of-plane bending mode remain even more significant w.r.t. the values based on TAU-LFD.

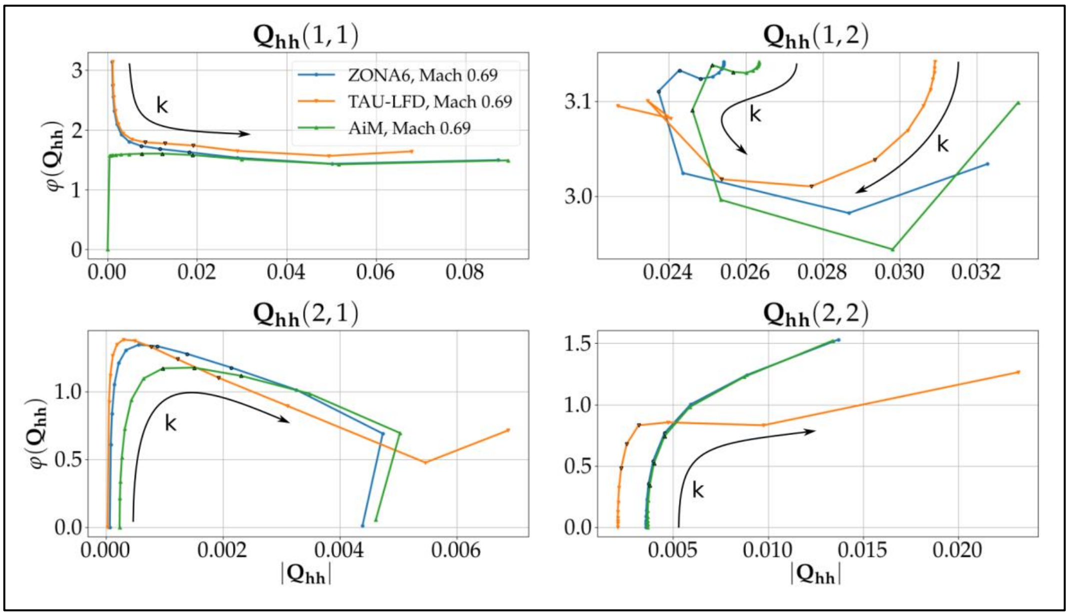

Figure 9: Comparison of GAF matrix entries between ZONA6, TAU-LFD, and AiM at a Mach number of 0.69

4.4 Aerodynamic Modal Power Transfer

Figure 10 displays the modal power transfer values for the two mode shapes of interest depending on the used methods and the two considered Mach numbers. The first two figure rows depict the matrix rows (normalized by the maximum absolute value of the matrices for the three methods) while the third figure row illustrates the column-wise sum of the absolute matrix values (normalized with the maximum value of each column sum).

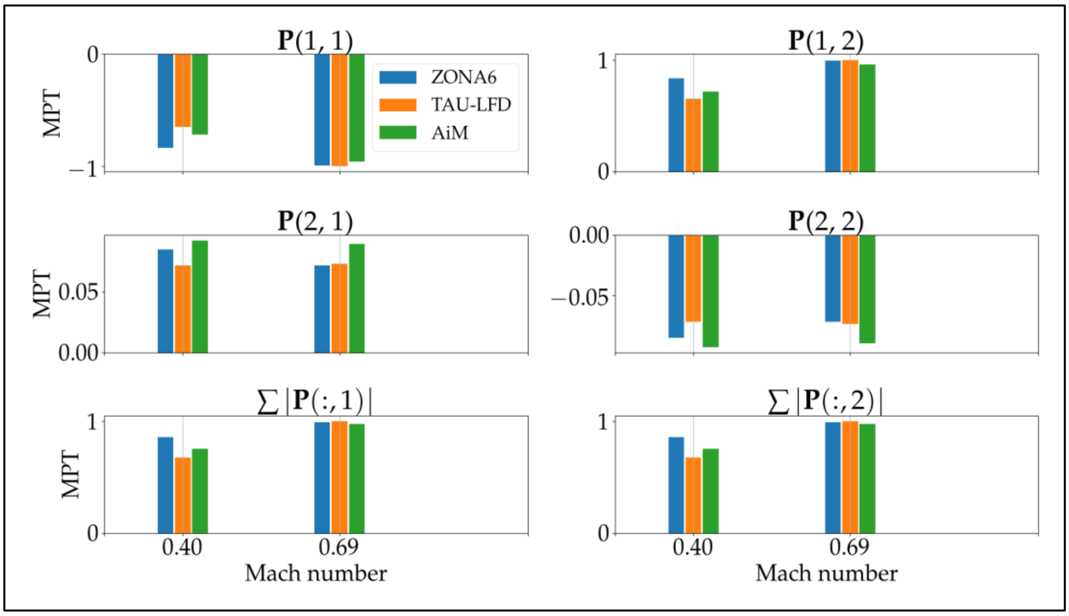

Figure 10: Modal Power Transfer between the VTP out-of-plane bending mode and the VTP torsion mode for Mach numbers of 0.40 and 0.69

For a Mach number of 0.4, the enhancement of generalized aerodynamic forces from ZONA6 by the AiM approach yields totaled modal aerodynamic power transfer values for each mode much closer to the TAU-LFD results in comparison to ZONA6 (last figure row). The individual matrix components, however, reveal an overestimation of the aerodynamic power transfer from the VTP out-of-plane bending on the VTP torsion (second row, first column, $\boldsymbol{P}(2,1)$) and from the VTP torsion on itself (second row, second column, $\boldsymbol{P}(2,2)$). A similar pattern can be observed for a Mach number of 0.69, but the total effect of the enhancement is less distinctive.

5 DISCUSSION

As documented by Figure 7 and Table 4, the enhancement of the linear potential flow theory based unsteady aerodynamics by forces induced by HTP inplane and roll motion results in an improvement of the flutter point prediction w.r.t. the linearized frequency domain CFD approach for the considered Mach numbers. A comparison of the GAF matrices with high-fidelity results reveals both, the strengths and weaknesses of the examined potential flow theory enhancement approach.

A sole modification of the real part concerning the aerodynamic influence of the VTP out-of-plane bending mode (HTP roll) on itself ($\boldsymbol{Q_{hh}}(1,1)$) results in a reduced mismatch between the amplitudes computed by ZAERO and TAU-LFD. This improvement, however, is only of minor magnitude. Since the imaginary component is not being modified by the approach as is (cf. Eq. (19)), a change in phase angle is the result. A possible extension of the enhancement approach could be the inclusion of roll damping, which would directly affect this matrix entry in amplitude and phase angle. Nevertheless, regarding the related MPT value ($\boldsymbol{P}(1,1)$), the approach as is yields a reasonable correction.

The amplitude discrepancy at zero reduced frequency in the aerodynamic influence of the VTP torsion mode (HTP inplane) on the VTP out-of-plane bending mode (HTP roll) ($\boldsymbol{Q_{hh}}(1, 2)$) is addressed by the AiM approach via the product of the change in strip lift due to sideslip angle $\partial l(y)/\partial\beta$ and the modal strip yaw angle ψ_0 (Eq. (20)) for unswept lifting surfaces. There still remains a significant difference to the TAU-LFD results, especially for the test case at a low transonic Mach number of 0.69. At quasi-steady state, the remaining amplitude offset might suggest inaccuracies in the computation of the change in strip lift due to sideslip angle. The related MPT value ($\boldsymbol{P}(1, 2)$), however, shows a reasonable change in aerodynamic power transfer to the VTP torsion mode (HTP inplane).

The aerodynamic influence of the VTP out-of-plane bending mode (HTP roll) on the VTP torsion mode (HTP inplane) ($\boldsymbol{Q_{hh}}(2, 1)$) experiences a strong modification of the phase angle and only a minor change in amplitude. Being of same magnitude as the roll moment due to yaw [17], a more comprehensive approach would also take the additional yaw moment due to roll into account. A further extension of the approach in this direction seems necessary regarding the related MPT value ($\boldsymbol{P}(2, 1)$).

The aerodynamic influence of the VTP torsion mode (HTP inplane) on itself ($\boldsymbol{Q_{hh}}(2, 2)$) is modified negligibly by the AiM approach. As this could only result from unsteady chordwise forces and yawing moments induced by the inplane motion, which are currently not considered by the method as is, this is reasonable. Regarding the related MPT value ($\boldsymbol{P}(2, 2)$), a similar necessity for an extension of the method as discussed for $\mathbf{P}(2, 1)$ seems reasonable. The relevance of chordwise forces for T-tail flutter is emphasized in [2].

6 CONCLUSION AND OUTLOOK

The comparative study shows the gain in accuracy for T-tail flutter point prediction obtained by employing a simple strip theory approach based on steady CFD forces in addition to common linear potential flow theory. The negligence of aerodynamic loads induced by lifting surface inplane and roll motion seems to be the main driver for the large deviations between the results based on the ZONA6 method and TAU-LFD. The addition of these forces generated by the strip theory approach reduces this deficit and supports a more precise flutter point prediction for the studied test case.

A further comparison of the modified GAF matrices and aerodynamic Modal Power Transfer values reveals shortcomings, which seem to be largely attributed to neglected drag force and yaw moment components induced by stabilizer roll and inplane motion. Nevertheless, considering the total aerodynamic Modal Power Transfer between the structural modes involved in the flutter mechanism, the AiM method reasonably approaches the mismatch between ZONA6 and TAU-LFD with some weak points at higher Mach numbers.

Regarding the additional aerodynamic forces generated by the strip theory approach as differential complex pressure distributions, the approach is limited to a constant change in pressure coefficient in chordwise direction, which might be a reason for inaccuracies in the computation of the change in strip lift due to sideslip angle. With an extension of the linear potential flow theory based aerodynamic forces on aerodynamic box level, as presented in [18], a better resolution of the additional pressure distribution in chordwise direction could be possible.

Additionally, the current study does neither consider roll damping nor drag components induced by stabilizer roll and inplane motion, although especially the latter appears to be significant for T-tail flutter. A modification of the present approach in this respect is aimed for.

Finally, for a more comprehensive flutter assessment of T-tails, structural preloading and quadratic mode shape components need to be considered. The former leads to a change in structural stiffness depending on the flight state, while the latter should be accounted for when including the additional side forces due to HTP roll, as suggested in [18].

7 REFERENCES

[1] W. Jennings and M. Berry, "Effect of Stabilizer Dihedral and Static Lift on T-Tail Flutter," *Journal of Aircraft,* pp. 364-367, 1977.

[2] J. Murua, L. van Zyl and R. Palacios, "T-Tail flutter: Potential-flow modelling, experimental validation and flight tests," *Progress in Aerospace Sciences,* pp. 54-84, 2014.

[3] "TAU-Code Users Guide," 2018.

[4] "MSC Nastran 2017 Dynamic Analysis User's Guide".

[5] "ZAERO Theoretical Manual".

[6] R. Thormann, "Accurate and Efficient, Time-linearized Flutter Analysis of Transport Aircraft," 2018.

[7] A. De Boer, M. S. Van der Schoot and H. Bijl, "Mesh deformation based on radial basis function interpolation," *Computers & structures,* vol. 85, pp. 784-795, 2007.

[8] A. Michler and R. Heinrich, "Numerical simulation of the elastic and trimmed aircraft," in *New Results in Numerical and Experimental Fluid Mechanics VII*, Springer, 2010, pp. 109-116.

[9] T. Theodorsen, "General Theory of Aerodynamic Instability and the Mechanism of Flutter," 1935.

[10] M. J. Queijo, "Theory For Computing Span Loads and Stability Derivatives Due to Sideslip, Yawing, and Rolling for Wings in Subsonic Compressible Flow," 1968.

[11] P. C. Chen, "Damping Perturbation Method for Flutter Solution: The g-Method," *AIAA*, vol. 38, pp. 1519-1524, 9 2000.

[12] H. Gödel, "Recent developments in: structural optimization with respect to dynamic and aeroelastic problems," in *Proceedings of the "International Forum on Aeroelasticity and Structural Dynamics", Aachen*, 1991.

[13] D. Schäfer, C. Vidy, C. Mack and J. Arnold, "Assessment of body-freedom flutter for an unmanned aerial vehicle," *CEAS Aeronautical Journal,* 12 2018.

[14] P. Schreiber, C. Vidy, A. Voß, J. Arnold and C. Mack, "Dynamic Aeroelastic Stability Analyses of Parameterized Flying Wing Configurations," in *Deutscher Luft- und Raumfahrtkongress*, 2018.

[15] "ZAERO User's Manual".

[16] National Oceanic and Atmospheric Administration, United States Air Force, US standard atmosphere, 1976, vol. 76, National Oceanic and Atmospheric Administration, 1976.

[17] W. P. Rodden, "Comment on 'Effect of Stabilizer Dihedral and Static Lift on T-Tail Flutter'," *Journal of Aircraft,* vol. 15, pp. 447-448, 7 1978.

[18] L. van Zyl and E. H. Mathews, "Aeroelastic Analysis of T-Tails Using an Enhanced Doublet Lattice Method," *Journal of Aircraft,* vol. 48, pp. 823-831, 5 2011.

COPYRIGHT STATEMENT

This project has received funding from the Clean Sky 2 Joint Undertaking under the European Union's Horizon 2020 research and innovation programme under grant agreement No 807097 - LPA GAM 2018 - H2020 - IBA-CS2-GAMS-2017.